Understanding the role of metal and N species in M@NC catalysts for electrochemical CO_2 reduction reaction

Manfen Liang, Yu Liu, Jie Zhang, Fangyuan Wang, Zhichao Miao [*], Lechen Diao, Jinglin Mu, Jin Zhou [*], Shuping Zhuo [*]

School of Chemistry and Chemical Engineering, Shandong University of Technology, Zibo 255000, PR China

ARTICLE INFO

ABSTRACT

The electrochemical CO_2 reduction reaction (CO_2RR) that transforms CO_2 to CO has attracted great interest. Transition metal nanoparticles encapsulated in nitrogen-doped carbon (M@NC) catalysts exhibit outstanding catalytic performance. However, the role of metal and N species in M@NC catalysts remains unclear. In this work, Co@C, Co@NC, Ni@C, and Ni@NC catalysts were achieved and employed in CO_2RR. The Ni@NC catalyst exhibits an industry level current density of 220 mA cm^{-2} and a high Faradaic efficiency of 98% for CO production at -0.87 V *vs.* RHE for 100 h. In addition, the N species, especially the pyrrolic-N in the shell of Ni@NC material provide active sites for adsorbing and activating CO_2 molecules, and metal nanoparticles improve the electronic structure of N species, thereby decreasing their ability for radical attack (*COOH, *CO, and *H). Consequently, this work can guide the design of M@NC catalyst for CO_2RR to CO.

1. Introduction

The ever-growing CO_2 concentration in the atmosphere is causing serious environmental crisis. The method for transforming CO_2 to high value-added chemicals plays a remarkable role in realizing carbon cycling and carbon neutrality, drawing increasing attention in recent years [1–5]. Among different methods for utilizing CO_2, the electrochemical CO_2 reduction reaction (CO_2RR) can transform CO_2 to CO, HCOOH, CH_3OH, and C_2H_5OH [6–8]. As for the products of CO_2RR, the CO is considered as the closest one to commercialization, which can be used in Fischer-Tropsch process to generate different fuels and chemicals [9,10]. Typically, CO_2RR proceeds in aqueous electrolyte, where hydrogen evolution reaction (HER) easily occurs, which decreases the selectivity of CO [8,11]. Thus, a catalyst with high product selectivity (Faradaic efficiency, FE), large current density, and long-term stability should be developed for industrialization.

In recent years, various types of catalysts, such as metal catalysts (noble and non-noble metals) [12,13], metal-based composite catalysts (oxides, sulfides, and M–N–C) [14–18], and metal-free catalysts [19,20] have been achieved and used in CO_2RR that converts CO_2 to CO. Au and Ag catalysts exhibit outstanding catalytic performance owing to their poor activities in HER [21,22]. However, high cost and low reserve have seriously restrained the utilization in CO_2RR. As for the metal-free

catalyst, low current density usually exists and limits their industrial application. Earth-rich transition metal-carbon composites have fascinating activities and are potential alternatives [23–26].

One of the most prominent non-precious metal electrocatalysts for converting CO_2RR to CO is transition metal trapped in nitrogen-doped carbon (M@NC), which has drawn attention owing to its low-cost and remarkable catalytic activity. Yuan et al. synthesized nitrogen doped nanotubes hybrid substrates through the *in-situ* encapsulation of Ni nanoparticles into N-doped nano-hybrid carbon substrates. By introducing the Ni nanoparticles, the N–C material exhibits enhanced performance and excellent long-term stability towards catalyzing CO_2 into CO [27]. He et al. developed a low-temperature chemical vapor deposition strategy to prepare a sheet-like open nanostructure with Ni nanoparticle wrapped by Ni–N species dispersed carbon layer (Ni–NC@Ni). The Ni–N species were considered as the active center and the conductive Ni core and sheet like hierarchical nanostructure enhance the electron transport and mass transfer during catalysis by providing the faster transfer path and plenty of open spaces [28]. Carbon-encapsulated catalysts exhibit enormous potential in CO_2RR, however, their application is still at preliminary stages, and they should be investigated in depth. More importantly, the genuine role of metal and N species in CO_2RR is still controversial despite these issues' importance for improving the application of M@NC in CO_2RR [29–32].

* Corresponding authors.
E-mail addresses: miaozhichao@sdut.edu.cn (Z. Miao), zhoujin@sdut.edu.cn (J. Zhou), zhuosp_academic@yahoo.com (S. Zhuo).

Herein, to investigate the role of metal and N species in CO_2RR, we developed four kinds of metal nanoparticles encapsulated within carbon shells (Co@C, Co@NC, Ni@C, and Ni@NC) composites. The textural properties, chemical bonds, and catalytic activities of the composites were minutely researched. A wrapped structure was successfully obtained, and the Ni@NC catalyst exhibited high activity and stability in CO_2 reduction, producing a specific current of 22.0 mA cm^{-2} and FE$_{(CO)}$% of 92% at − 0.97 V *vs.* RHE. In a flow cell system, the Ni@NC catalyst exhibited an industry level current density of 220 mA cm^{-2} and a high FE of 98% for CO production at − 0.87 V *vs.* RHE. Density functional theory (DFT) calculations confirmed that the adsorption and activation of CO_2 molecules mainly occurred on the N species in the shell of the catalyst. The encased metal nanoparticles improved the electronic structure of the N species, thereby decreasing their adsorption energy for *COOH and *CO and enhancing the catalytic performance in CO_2RR. This work provides a new insight to develop the carbon-encapsulated catalysts and promotes their application in CO_2RR.

2. Experiment section

2.1. Chemicals and reagents

Cobalt nitrate hexahydrate (Co(NO$_3$)$_2$·6H$_2$O), nickel nitrate hexahydrate (Ni(NO$_3$)$_2$·6H$_2$O), zinc nitrate hexahydrate (Zn(NO$_3$)$_2$·6H$_2$O), 2-methylimidazole (C$_4$H$_6$N$_2$, 2-MI), trimesic acid (C$_9$H$_6$O$_6$, H$_3$BTC), PVP ((C$_6$H$_9$NO)$_n$, M$_w$ = 130000), methanol (CH$_3$OH), ethanol (C$_2$H$_5$OH), N, N-dimethylformamide (C$_3$H$_7$NO, DMF), potassium bicarbonate (KHCO$_3$), potassium hydroxide (KOH), and potassium thiocyanate (KSCN) were purchased from Aladdin Chemistry Co. Ltd. All the chemicals were used as supplied. Deionized water was filtered with a Millipore purification system (resistivity = 18.2 MΩ).

2.2. Synthesis of materials

2.2.1. Synthesis of Co-BTC material [33]
Co(NO$_3$)$_2$·6H$_2$O (0.582 g) and H$_3$BTC (0.150 g) were dissolved in 35 mL of DMF solvent and stirred at room temperature for 2 h. The obtained light pink solution was then sealed in a Teflon autoclave (50 mL) and maintained at 120 °C for 24 h. The resulting precipitate was centrifuged, washed, and dried. The obtained light purple powder is denoted as Co-BTC.

2.2.2. Synthesis of Co-2-MI material [34,35]
Co(NO$_3$)$_2$·6H$_2$O (0.291 g) was dissolved in 25 mL of methanol. Subsequently, 2-MI (1.642 g) was dissolved in 25 mL of methanol and then poured in the pink cobalt solution. The mixed aqueous solution was stirred at room temperature for 24 h. The resulting precipitate was centrifuged, washed, and dried. The obtained purple powder is denoted as Co-2-MI.

2.2.3. Synthesis of Ni-BTC material [36,37]
Ni(NO$_3$)$_2$·6H$_2$O (0.432 g), H$_3$BTC (0.150 g), and PVP (1.5 g) were dissolved in 30 mL of a mixture solution (distilled water: ethanol: DMF = 1:1:1 v/v/v) and vigorously stirred at room temperature for 1 h. The obtained light green solution was then transferred to a 50 mL Teflon autoclave and heated to 150 °C for 10 h. The resulting precipitate was centrifuged, washed, and dried. The obtained light green powder is denoted as Ni-BTC.

2.2.4. Synthesis of Ni-2-MI material [33]
Ni(NO$_3$)$_2$·6H$_2$O (0.291 g) was dissolved in 20 mL of methanol. Then, 2-MI (1.642 g) was dissolved in 20 mL of methanol and introduced to the green nickel nitrate solution. The mixed aqueous solution was vigorously stirred at room temperature for 1 h. The obtained mixture was heated to 140 °C for 12 h in a 50 mL Teflon autoclave. The resulting precipitate was centrifuged, washed and dried. The obtained yellow

powder is denoted as Ni-2-MI.

2.2.5. Synthesis of Co@C, Co@NC, Ni@C and Ni@NC catalyst
The Co-BTC, Co-2-MI, Ni-BTC, and Ni-2-MI materials were placed in a tube furnace for carbonization in a N$_2$ atmosphere at 800 °C for 3 h at a heating rate of 2 °C min^{-1}. The as-obtained composites are denoted as Co@C, Co@NC, Ni@C, and Ni@NC.

2.3. Characterization

The X-ray diffraction (XRD) analysis was performed using a Bruker D8 Advance diffractometer with Cu Kα radiation (λ = 0.1541 nm) in a 2θ range of 5–90°. Scanning electron microscopy (SEM) and energy dispersive X-ray element mapping images were collected on a FEI Quanta FEG 250. The chemical state and composition of the materials were investigated through X-ray photoelectron spectroscopy (XPS, Thermo Fischer, ESCALAB 250Xi), and the binding energy was calibrated using the C1s peak at a value of 284.8 eV. The Fourier-transform Infrared (FT-IR) spectra of the samples were obtained using a Thermo Fisher Nicolet IS10 spectrometer at 4000–400 cm^{-1}. UV–visible (UV–vis) spectra were collected on UV 3600 (Shimadzu Corporation) in the range of 200–800 nm. Raman spectroscopy measurement was detected by a LabRam HR system equipped with a CCD detector and a 532 nm laser at 1 mW laser power. The nitrogen adsorption-desorption isotherms and CO$_2$-physisorption were recorded at − 196 °C and 0 °C on Micromeritics 3-Flex Physisorption (Micromeritics Instrument) static volumetric analyzer with degassing samples (300 °C for 2 h). The surface area of the samples was estimated with the Brunauer-Emmett-Teller method. Transmission electron microscopy (TEM, FEI Tecnai G2 F20) and energy-dispersive X-ray spectroscopy were used in analyzing the surface morphology and elemental distribution of samples. Inductively coupled plasma-mass spectrometry (ICP-MS) was tested on an Agilent 7500ce.

2.4. Electrochemical measurements

The experiments were performed in a two-compartment electrochemical H-cell with a Nafion-115 proton exchange membrane (Dupont) as the separator. Both compartments were filled with 120 mL of 0.5 M KHCO$_3$ electrolyte. Electrocatalytic measurements were carried out in a three-electrode system at a CHI760E electrochemical analyzer (CH Instruments, Inc., Shanghai). The Ag/AgCl (saturated by KCl) and Pt mesh were used as reference and counter electrodes, respectively. Potentials were calibrated according to the following equation: E (*vs.* RHE) = E (*vs.* Ag/AgCl) + 0.1989 V + 0.0592 × pH (pH = 7.2). In the preparation of the working electrode, 5 mg of catalysts were dispersed in a solution of 50 µL of Nafion solution and 2450 µL of DMF by ultrasonic dispersion for 2 h. Then, 100 µL of the resulting catalyst ink was dropped to a carbon paper (1.0 × 0.5 cm^2) with mass loading of 0.2 mg cm^{-2}. CO$_2$ gas at a flow rate of 10 mL min^{-1} was introduced to the cathode chamber for 0.5 h to saturate electrolyte before electrolysis. The electrolyte in the cathode chamber was agitated during measurement. The gas-phase products were diverted and analyzed with an online gas chromatograph (GC-2014, Shimadzu) equipped with a thermal conductivity detector (TCD) and a methanizer assisted flame ionization detector (FID). The liquid-products were confirmed with a ^{1}H nuclear magnetic resonance (^{1}H NMR) spectrometer (Bruker AVANCE III 400), and dimethyl sulfoxide (DMSO) was used as the internal standard.

The FE of product under different applied potentials was obtained with the following equation:

$$FE_i = \frac{Z_i \times V_i \times G \times F \times P_o}{I \times R \times T_o}$$

where, Z_i is the number of transferred electrons for gas product formation (two for CO and H$_2$), V_i is the volume ratio of generated gas from the

cathodic compartment, G is the gas flow rate (10 mL min^{-1}) controlled by a digital flow controller under ambient pressure, F is the Faradaic constant (96,485 C mol^{-1}), P_0 is the atmospheric pressure (1.013×10^5 Pa), I is the measured current under different applied potentials, R is the molar gas constant (8.314 J mol^{-1} K^{-1}), and T_o is the reaction temperature (298 K).

In the flow cell tests, the catalyst-coated gas diffusion electrodes (GDEs), Ag/AgCl, and Pt sheets (1.5 cm × 3.5 cm, 2 mm thickness) were employed as the working electrode, reference electrode, and counter electrode, respectively. The cathodic and anodic chambers were divided with an anion exchange membrane (Fumasep, FAA-3PK-130). The three components were positioned and clamped together with polytetrafluoroethylene spacers. CO_2 flow was controlled at 20 mL min^{-1} by using a mass flow controller, and the mass loading of the catalyst was 1 mg cm^{-2}. KOH (1M) was used as the electrolyte, and the electrolyte flow was kept at 10 mL min^{-1} with peristaltic pumps (Gaoss Union EC200–01) equipped with a silicone tubing. The products were detected and quantificationally analyzed using the above method.

Linear sweep voltammetry (LSV) was performed in Ar or CO_2-saturated 0.5 M KHCO$_3$ with the scan rate of 5 mV s^{-1} from 0 to − 1.3 V *vs.* RHE. The electrochemical surface area (ECSA) of catalyst was calculated from the electrochemical C_{dl}. Cyclic voltammogram measurements were performed under the potential range from 0.20 V to 0.30 V *vs.* RHE under CO_2 atmosphere at scan rates of 10–60 mV s^{-1} for the calculation of the C_{dl} of each catalyst ($\Delta j = j_a - j_c$ at 0.25 V *vs.* RHE in which j_c and j_a are the cathodic and anodic current densities, respectively). The electrochemical impedance spectra (EIS) of the electrodes were collected with by an electrochemical workstation (PARSTAT 4000) with AC voltage of 5 mV amplitude within the frequency range of 0.01–10 kHz.

2.5. Investigation of the active site

2.5.1. Acid-treatment of the Ni@NC catalyst

70 mg of Ni@NC catalyst was treated with 1M HCl (25 mL) at 60 °C for 6 h and 1M HNO$_3$ (25 mL) at 60 °C for 6 h for the removal of metal particles on the surface of the catalyst. Subsequently, the catalyst was washed with deionized water to remove adsorbed ions. Finally, the catalyst was dried at 70 °C overnight and treated at 700 °C for 3 h in N$_2$ atmosphere for the removal of adsorbed H$_2$O.

2.5.2. Poisoned by SCN$^-$

The SCN$^-$ was selected as the poisoning agent for the investigation of the active site. The LSV and electrocatalytic activity of Ni@NC were tested in the presence of 0.05M KSCN in 0.5M KHCO$_3$ electrolyte.

2.5.3. Poisoned by H$_3$PO$_4$

The as-synthesized Ni@NC working electrode was immersed in 1M H$_3$PO$_4$ aqueous solution at 60 °C for 6 h and dried at 60 °C overnight. The catalytic performance of Ni@NC poisoned by H$_3$PO$_4$ was investigated using the above method.

2.5.4. Synthesis of C and NC materials

The C and NC materials were synthesized using Zn(NO$_3$)$_2$·6H$_2$O as a metal source, which evaporates at high temperatures to form a metal-free material.

The Zn(NO$_3$)$_2$·6H$_2$O (0.440 g) and H$_3$BTC (0.150 g) were stirred in 30 mL of a mixture solution (distilled water: ethanol: DMF = 1:1:1 v/v/v) at room temperature for 1 h. The obtained solution was then placed in a 50 mL Teflon autoclave and heated at 150 °C for 10 h. The white precipitate was centrifuged, washed, and dried, which is denoted as Zn-BTC.

Zn(NO$_3$)$_2$·6H$_2$O (0.461 g) was dissolved in 3 mL of deionized water. Subsequently, 2-MI (5.50 g) was dissolved in 20 mL of deionized water. The two solutions were mixed and stirred at room temperature for 6 h. The as-obtained precipitate was centrifuged, washed, and dried. The as-obtained powder is denoted as Zn-2-MI.

Zn-BTC and Zn-2-MI were placed in a tube furnace for carbonization at 800 °C for 3 h at a heating rate of 2 °C min^{-1} under N$_2$ atmosphere. The obtained composites are denoted as C and NC, respectively.

2.6. DFT calculation

First-principles calculations were carried out with Dmol as implemented in the Materials Studio 2019, using Perdew-Burke-Ernzerhof (PBE) generalized gradient approximation, D2 dispersion correction and double numeric polarized (DNP) basis set [38,39]. The geometries were relaxed until the residual forces were less than 0.04 eV/Å. Co(111) slab and Ni(111) slab with three layers were created by the face-centered cubic bulk structure, and each layer contained 16 atoms. After the optimization of the two slab models and the 4 × 4 graphene supercell, a carbon-coated metal particle was constructed with 15 Å of vacuum and simulated by fixing metal atoms with 5 × 5 × 1 Monkhorst-Pack mesh of k-points. The free energy curves of the computational hydrogen electrode model were adopted to describe electrochemical reaction steps. Considering PBE inaccuracies in the enthalpy and solvation correction in the experimental reaction, 0.51 eV, − 0.25 eV, and − 0.1 eV were added to CO gas molecules, *COOH, and *CO, respectively [40]. The final free energy including zero-point energy (ZPE), enthalpy, and entropy were further calculated as follows [41]:

$$\Delta G_{*COOH} = E(*COOH) - E(*) - 1/2E(H_2(g)) - E(CO_2(g)) + \Delta ZPE + \Delta H - T\Delta S - eU$$

$$\Delta G_{*CO} = E(*CO) + E(H_2O(l)) - E(*CO) + 1/2E(H_2(g)) + \Delta ZPE + \Delta H - T\Delta S - eU$$
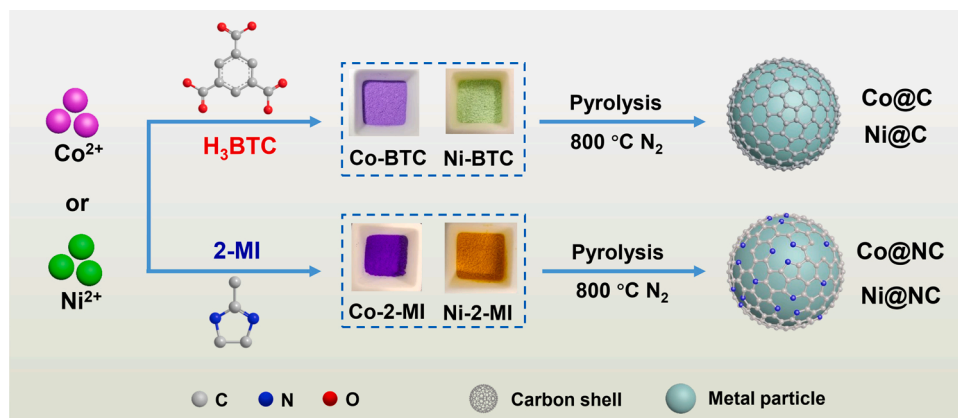
In the above equations, E is the total electronic energy, the ZPE, enthalpy, and entropy represent contributions from the calculated vibrations of surface species at 298 K (S).

3. Results and discussion

3.1. Characterizations of Co-BTC, Co-2-MI, Ni-BTC, and Ni-2-MI materials

The synthetic procedure of M@NC composites is displayed in Scheme 1. The role of metal was investigated by comparing different kinds of metals (Co and Ni species). In addition, ligands without N species (H$_3$BTC) and with N species (2-MI) were selected to synthesize the metal-ligand (M-L) complex. Guided by this thought, four kinds of Co-BTC, Co-2-MI, Ni-BTC, and Ni-2-MI materials were designed and obtained. In the pyrolysis process, the coordination bonds between metal ions and organic ligands were destroyed. At the same time, the metal ions were reduced and aggregated to metal particles, and the ligands were carbonized to carbon shells around the metal particles [29, 33]. Four kinds of metal particles encapsulated within carbon shells (Co@C, Co@NC, Ni@C, and Ni@NC) composites were achieved.

The as-synthesized M-L materials were investigated through XRD, SEM, XPS, FT-IR, and UV–vis characterizations. As shown in Fig. 1a–d, obvious diffraction peaks, which are consistent the reported literature [33,37,42,43], are detected in the XRD patterns, implying the successful synthesis of Co-BTC, Co-2-MI, Ni-BTC, and Ni-2-MI materials. In addition, the SEM images in the inset of Fig. 1a–d show the smooth surfaces of the obtained materials, and the elemental mappings (Fig. S1) imply the successful introduction of objective elements. Furthermore, the XPS spectra were obtained to confirm the chemical bonds in the materials. The content of different elements is provided in Table S1. As displayed in the C 1 s spectra (Fig. 1e,i), C—C (284.8 eV) and O—C=O (288.5 eV) bonds are detected in the Co-BTC and Ni-BTC materials [44], and only C—C (284.8 eV) and C—N (291.3 eV) bonds are observed in the Co-2-MI and Ni-2-MI materials [45]. In addition, obvious differences can be observed in the N 1 s (Fig. 1f,j) and O 1 s (Fig. 1g,k) spectra. More precisely, obvious Co—N and Ni—N bonds (398.8 eV) are detected in

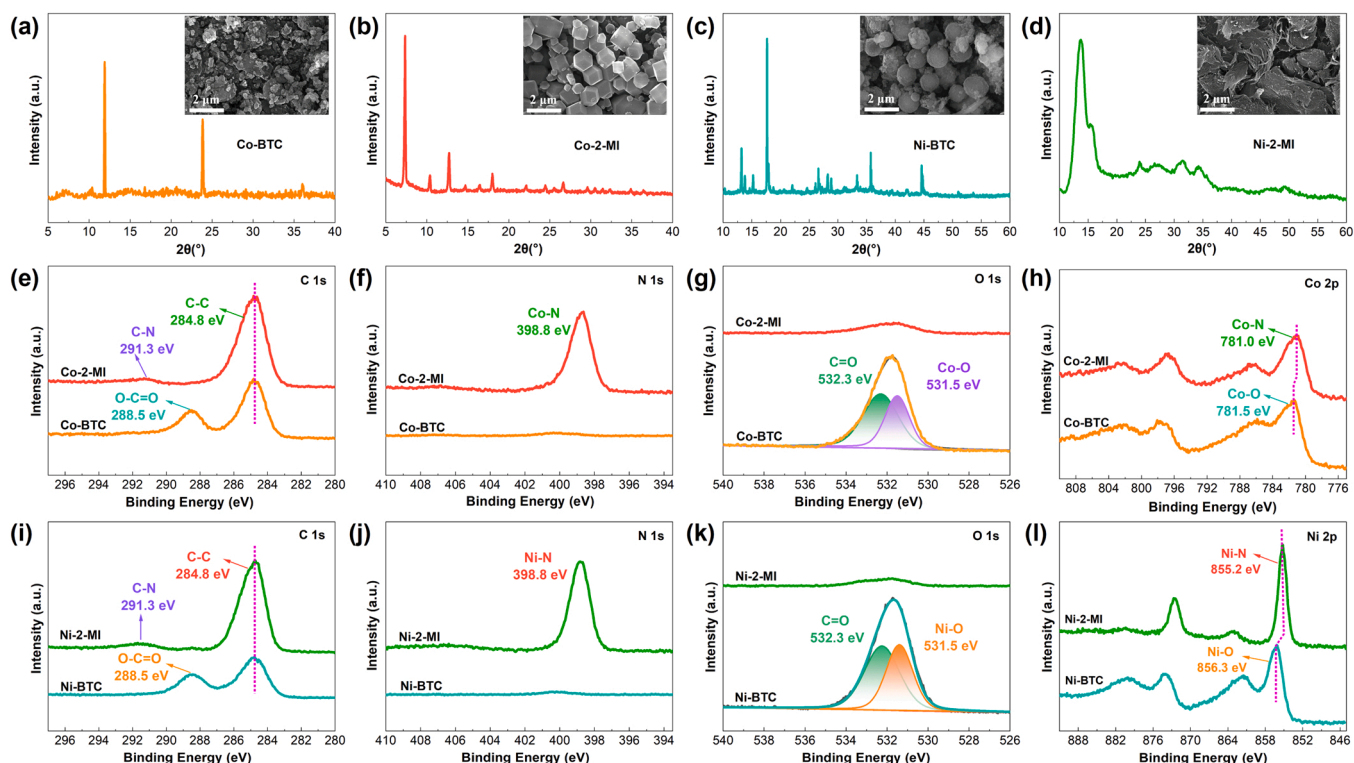**Scheme 1.** The synthetic procedure of M@NC composites.

Fig. 1. (a-d) XRD patterns and SEM images, (e, i) C 1 s XPS spectra, (f, j) N 1 s XPS spectra, (g, k) O 1 s XPS spectra, (h) Co 2p XPS spectra, and (l) Ni 2p XPS spectra of Co-BTC, Co-2-MI, Ni-BTC, and Ni-2-MI materials.

the Co-2-MI and Ni-2-MI materials, and obvious C=O (532.3 eV) and M—O bonds (531.5 eV) exist in the Co-BTC and Ni-BTC materials [46, 47]. As for the Co 2p and Ni 2p spectra (Fig. 1h,l), the Co and Ni species are present as Co—O (781.5 eV) and Ni—O (856.3 eV) bonds in the Co-BTC and Ni-BTC materials [48,49]. By contrast, only Co—N (781.0 eV) and Ni—N (855.2 eV) bonds exist in the Co-2-MI and Ni-2-MI materials. The FT-IR spectra (Fig. S2a) of Co-BTC and Ni-BTC materials exhibit the –COO$^-$ (1620–1560 cm^{-1} and 1440–1370 cm^{-1}) [50,51] and M—O (470–420 cm^{-1}) bonds [52,53], and the Co-2-MI and Ni-2-MI materials provide the C—N and M—N bonds at 1000 cm^{-1} and 470–420 cm^{-1} [54,55]. Meanwhile, obvious peaks are detected at 200–800 nm of the UV–vis spectra (Fig. S2b), corresponding to the color of M-L materials (Scheme 1). All these characterizations draw a conclusion that the Co-BTC, Co-2-MI, Ni-BTC, and Ni-2-MI materials were successfully achieved as designed.

3.2. Characterizations of Co@C, Co@NC, Ni@C, and Ni@NC composites

After the thermal treatment of M-L materials at 800 °C, the M@NC (Co@C, Co@NC, Ni@C, and Ni@NC) composites were achieved and characterized through XRD, Raman, N$_2$-physisorption, XPS, TEM, and SEM techniques. As shown in the XRD patterns (Fig. 2a), the diffraction peaks of M-L materials vanish after the pyrolysis process. Meanwhile, obvious diffraction peaks of metal appear. For the Co@C and Co@NC composites, the peaks at 44.2°, 51.5°, and 75.8° are due to the metallic Co (JCPDS No. 15-0806) [56], and the weak peak at approximately 26° originates from the (002) reflection of graphitic carbon (JCPDS No. 41-1487) [36]. In addition, the obvious diffraction peaks of metallic Ni (JCPDS No. 04-0850) are detected at 44.5°, 51.8°, and 76.3° in the Ni@C and Ni@NC composites [30], implying that the metal ions in the M-L materials are reduced to metallic particles. No metallic nitrides and
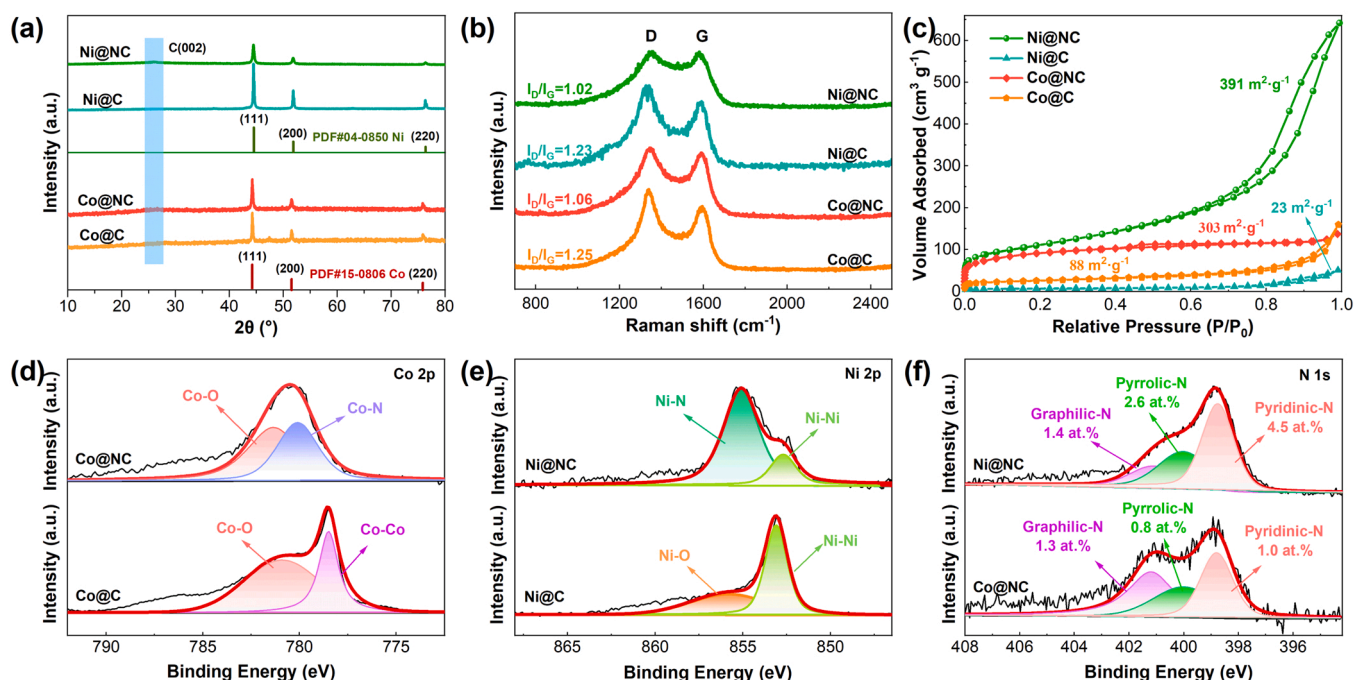
Fig. 2. (a) XRD patterns, (b) Raman spectra, (c) N₂-physisorption, (d) Co 2p XPS spectra, (e) Ni 2p XPS spectra, and (f) N 1 s XPS spectra of Co@C, Co@NC, Ni@C, and Ni@NC composites.

metallic carbides are identified in the XRD patterns.

As shown in the Raman spectra of M@NC (Fig. 2b), the characteristic signatures located at approximately 1350 and 1600 cm^{-1} are attributed to the D band (disoriented carbon) and G band (graphitic carbon), respectively [57,58]. The smaller I_D/I_G band intensity ratio of Co@NC (1.06) and Ni@NC (1.02) reveals the existence of more amounts of graphitic carbon than Co@C (1.25) and Ni@C (1.23) composites. The graphitic carbon is beneficial for the transmission of electrons in the electrocatalytic process [55].

The N₂-physisorption of Co@C, Co@NC, Ni@C, and Ni@NC composites were used in investigating the textural properties of the materials. As shown in Fig. 2c, typical I isotherms are observed, implying the existence of a microporous structure. Furthermore, distinct hysteresis loop is found in a P/P₀ range of 0.7–1.0 in the Ni@NC materials, implying the presence of large pore structure [59]. The abundant pore structure is beneficial for promoting mass transport capacity. The Co@C and Ni@C composites have low adsorption quantity and small specific surface area (88 m² g^{-1} and 23 m² g^{-1}). By contrast, Co@NC and Ni@NC composites have large specific surface areas (303 m² g^{-1} and 391 m² g^{-1}), which can provide additional active sites for the reactants.

The composites and chemical bonds of M@NC materials were characterized using XPS techniques. As shown in Fig. S3a,b, C, N, O, and M (Co or Ni) species are successfully introduced into the composites. The content of different elements is provided in Table 1. The low C content of Co@C and Ni@C composites is mainly owing to the existence of carboxyl and high O content in the Co-BTC and Ni-BTC materials, which consume the carbon source in the pyrolysis process. For the C 1 s spectra (Fig. S3c,d), C—C (284.8 eV), C—O/C═N (285.7 eV), and C═O/C—N

(289.3 eV) bonds are detected [60,61]. As for the metal species (Fig. 2d, e), Co—Co and Co—O bonds, which are ascribed to the metal Co particle and oxidation of surface metallic Co species, are observed at 778.5 eV and 780.9 eV in the Co@C composite [43]. In addition, the Co—O bond can be verified by the O 1 s spectra (Fig. S3e). However, only Co—N and Co—O bonds are detected in Co@NC composites, and the Co—N bond is owing to the interaction between metal Co particles and N-doped carbon shell. A similar trend is observed in the Ni@C (Ni—Ni and Ni—O bonds) and Ni@NC composites (Ni—Ni and Ni—N bonds). In the N 1 s spectra (Fig. 2f), different kinds of N species, such as pyridinic-N, pyrrolic-N, and graphitic-N are detected at approximately 398.8 eV, 400.0 eV, and 401.2 eV, respectively [62]. In addition, the N content, especially pyridinic-N and pyrrolic-N species in Ni@NC is higher than that in the Co@NC material, which might promote interactions between Ni and N species.

The morphology and encapsulated structure of the M@NC materials were characterized through TEM (Fig. 3a–d), HRTEM (Fig. 3e–h), and SEM (Fig. S4) images. Obvious metal particles are observed in the carbon skeleton. The Co@C and Co@NC composites have larger particle size than the Ni@C and Ni@NC composites. The elemental mappings (Fig. S5) imply the successful introduction of objective elements, and the metal particles are highly dispersed on the composites. In the HRTEM images (Fig. 3e–h), the encapsulated structure is clearly observed, suggesting the successful fabrication of Co@C, Co@NC, Ni@C, and Ni@NC composites. As for the core region, crystal plane spacing corresponds to the lattice plane (111) or (200) of Co or Ni particles. Conversely, the lattice fringes with approximately 0.33 nm crystal plane spacing in the shell region are ascribed to the lattice plane (002) of graphitic carbon

Table 1

Textural properties and composition of Co@C, Co@NC, Ni@C, and Ni@NC composites gotten from XRD, Raman, N₂-physisorption, and XPS measurements.

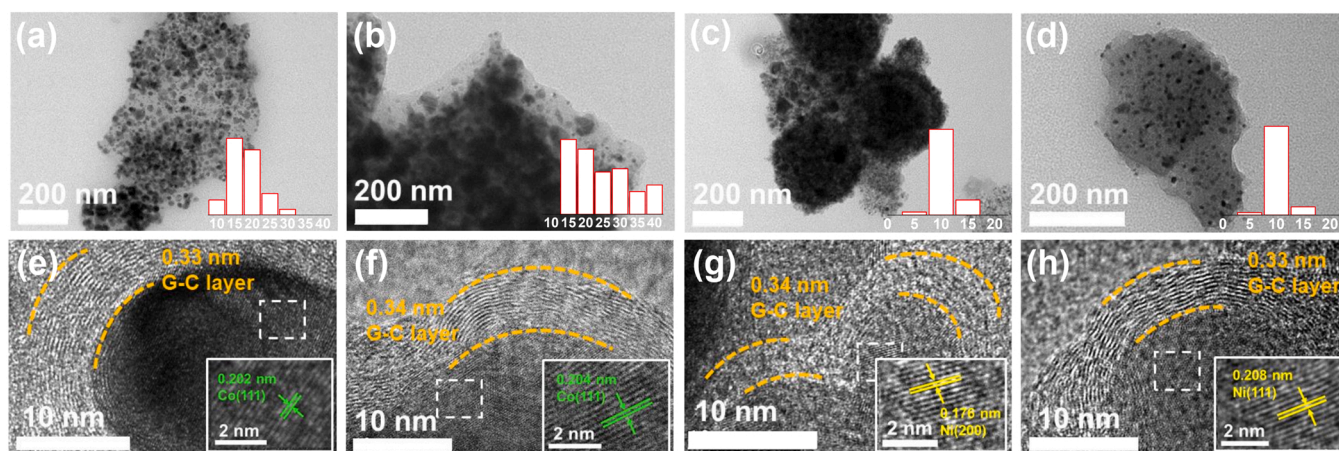| Sample	XRD		Raman	N₂-physisorption	XPS (at%)				
	Size (nm)	Interplanar space (nm)	I_D/I_G	S_{BET} (m² g^{-1})	C	N	O	Co	Ni
Co@C	37.4	0.205	1.25	88	75.5	–	13.1	11.4	–
Co@NC	31.5	0.205	1.06	303	82.1	3.1	10.3	4.5	–
Ni@C	39.3	0.203	1.23	23	70.6	–	12.0	–	17.4
Ni@NC	24.4	0.203	1.02	391	77.8	8.5	7.9	–	5.8

Fig. 3. TEM, HRTEM images, and particle size distributions of **(a, e)** Co@C, **(b, f)** Co@NC, **(c, g)** Ni@C, and **(d, h)** Ni@NC composites.

(G-C) phases.

3.3. Catalytic performance for CO₂RR

The obtained Co@C, Co@NC, Ni@C, and Ni@NC composites were employed as catalysts for CO₂RR, and their catalytic performance was studied systematically. First, the FE% of CO and H₂ of all the catalysts is provided (Fig. 4a,b). With regard to the products, only CO and H₂ are detected, and no liquid product is found (Fig. S6). As for the Co@C catalyst, no obvious CO is detected, and the $FE_{(H_2)}$% approaches 100%, implying the absence of active sites for CO₂RR. After the introduction of N species, the $FE_{(CO)}$% of Co@NC catalyst reaches approximately 28%, implying that the N species can provide active sites for CO₂RR to CO. A similar conclusion is obtained in the Ni@C and Ni@NC catalysts.
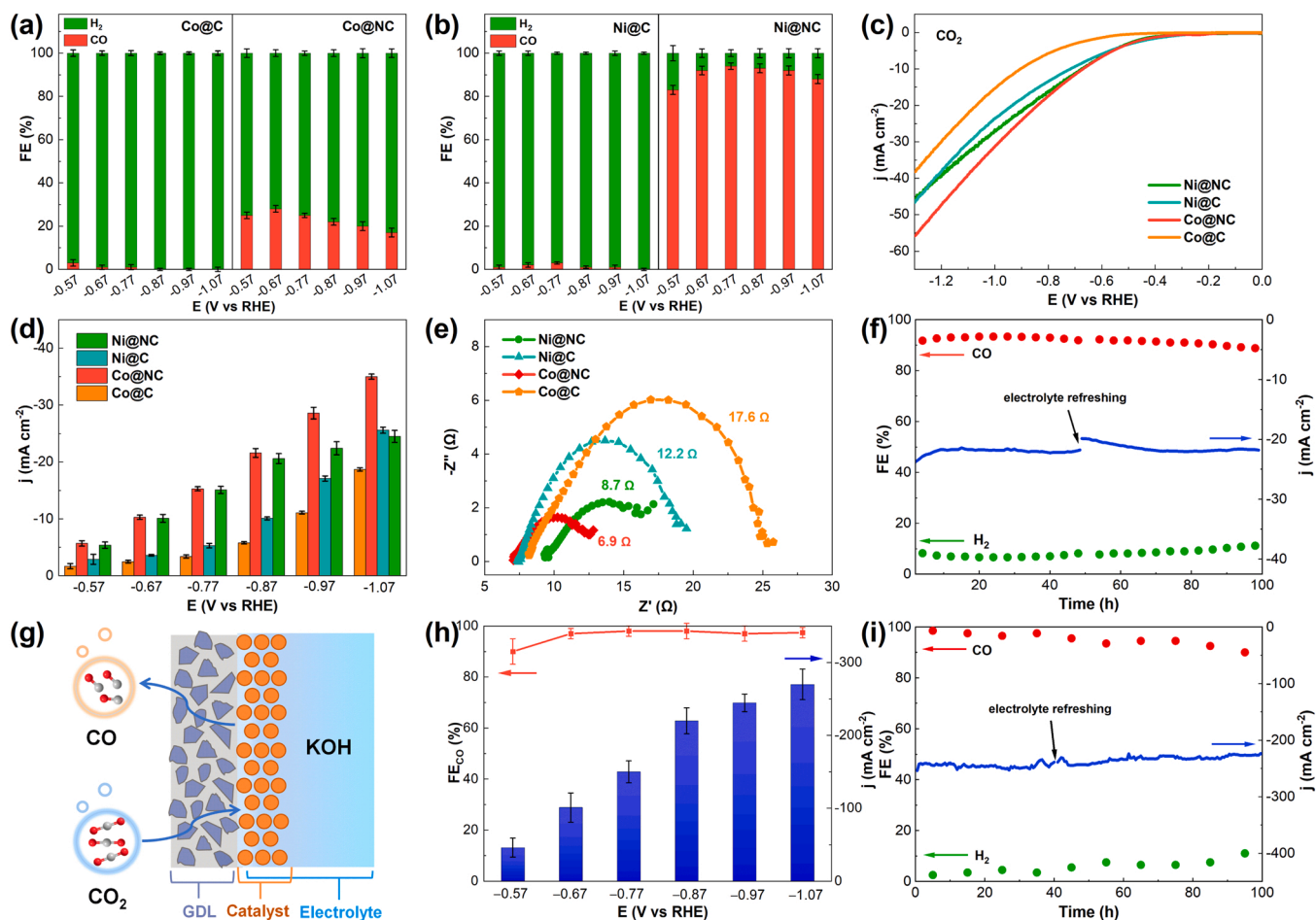

Fig. 4. Electrocatalytic performance: (a) $FE_{(CO)}$% and $FE_{(H_2)}$% with different applied potentials of Co@C and Co@NC, (b) $FE_{(CO)}$% and $FE_{(H_2)}$% with different applied potentials of Ni@C and Ni@NC, (c) LSV test, (d) Current density, (e) Electrochemical impedance spectra, (f) Long-term durability of Ni@NC at − 0.97 V for 100 h, (g) Schematic diagram of gas diffusion electrode, (h) Catalytic performance of Ni@NC at different applied potentials in the flow cell, and (i) Long-term durability of Ni@NC at − 0.87 V for 100 h in the flow cell.

Without N species, the Ni@C catalyst mainly promotes HER, and $FE_{(H2)}$% is approximately 100%. As for the Ni@NC catalyst, the $FE_{(CO)}$% can reach 95%, implying its excellent performance for CO_2RR to CO. Furthermore, the effect of metal in catalytic performance is investigated. It can be found that the Ni@NC catalyst exhibits distinctly higher $FE_{(CO)}$% than the Co@NC catalyst, implying that the Ni species promote the improvement of catalytic performance.

The LSV profiles under Ar and CO_2 atmosphere were tested and provided in Fig. S7. After the introduction of CO_2 atmosphere, no increase in current response is observed for Co@C and Ni@C catalysts. As for the Co@NC catalyst, the current density is enhanced under CO_2 atmosphere. Furthermore, a remarkable increase in current density is observed in the Ni@NC with the introduction of CO_2 atmosphere, suggesting excellent activity for CO_2RR. The results obtained from LSV are consistent with the change law of $FE_{(CO)}$%. Furthermore, the current density of Co@C, Co@NC, Ni@C, and Ni@NC catalysts was investigated. As shown in Fig. 4c,d, the Co@NC and Ni@NC catalysts exhibit higher current density than the Co@C and Ni@C catalyst under low overpotential (-0.57 V to -0.97 V). Under a large potential, the current density of Ni@C increases mainly because of HER.

The differences in catalytic performance among the samples were investigated. The influencing factors for FE% and current density were determined through CO_2 adsorption, ECSA, Tafel slope, and EIS electrochemical characterizations. According to the measured CO_2 adsorption isotherms in Fig. S8, the CO_2 adsorption capacity of Co@NC and Ni@NC catalysts is higher than those of the Co@C and Ni@C catalysts, consistent with the specific surface area of the samples. Moreover, the Co@NC catalyst has a similar CO_2 adsorption capacity to Ni@NC. However, their $FE_{(CO)}$% values largely differ, implying that CO_2 adsorption capacity is not the key step for CO_2RR.

The ECSA values of the catalysts were detected and shown in Fig. S9. The Ni@NC catalyst owns the maximal C_{dl} (9.62 mF cm^{-2}), implying that it can offer the highest number of active sites for CO_2 molecules [2, 62]. As a result, the Ni@NC catalyst possesses the highest $FE_{(CO)}$% value. The Co@C and Ni@C catalysts provide smaller C_{dl} (1.40 mF cm^{-2} and 3.26 mF cm^{-2}, respectively) than the Co@NC and Ni@NC catalysts.

The capacity for the transfer of electron was researched by Tafel slopes (Fig. S10). The Tafel slope of Ni@NC is approximately 118 mV dec^{-1}, implying that the first electron transferred to the CO_2 molecule is the rate-determining step of CO_2RR [11,15]. In addition, the higher value of Tafel slope (168 mV dec^{-1}) in Co@NC implies its larger resistance for electron transmission. In addition, the rate-determining step for Co@NC might be CO_2 adsorption to and/or CO desorption from active sites [63].

Furthermore, the EIS was conducted to research the properties of the electrode/electrolyte interface and reveal the interfacial charge-transfer resistance (R_{ct}) of the catalysts [15]. As shown in Fig. 4e, the semicircle diameter of EIS corresponds to R_{ct} values of 17.6 Ω, 12.2 Ω, 6.9 Ω, and 8.7 Ω for Co@C, Ni@C, Co@NC, and Ni@NC catalysts, respectively. For the catalysts with N species, low interfacial R_{ct} values are detected. The low interfacial R_{ct} benefits the transmission of electrons, resulting in a large current density for catalyst (Fig. 4c,d).

As an important parameter for evaluating prospect of catalyst in practical application, the long-term durability test of Ni@NC catalyst was performed. As shown in Fig. 4f and Fig. S11, little attenuation in catalytic performance ($FE_{(CO)}$% and current density) is observed after 100 h under -0.97 V, indicating the excellent stability of the Ni@NC catalyst in CO_2RR. Meanwhile, the metal content in the electrolyte after reaction was investigated by the ICP-MS. Little Ni species (1.8×10^{-4} mg kg^{-1}) are detected. In addition, the used Ni@NC electrode was investigated by XRD, Raman, and SEM characterizations (Fig. S12). No noticeable change in structural and chemical properties of Ni@NC is observed after reaction process, indicating the excellent stability of Ni@NC in CO_2RR.

In consideration of the CO_2 mass transport limitation in H-cell, flow cell equipped with GDE is widely investigated and expected to overcome

the above question [64,65]. In addition, 1 M KOH was used as an electrolyte to suppress HER. Therefore, we coated the Ni@NC catalyst on the GDE and investigated the CO_2RR performance in a flow cell system (Fig. 4g). In the flow cell system, the current density of Ni@NC catalyst increases with the enhancement of applied potentials, and it exhibits an industry level current density of 220 mA cm^{-2} and a high FE of 98% for CO production at -0.87 V *vs.* RHE (Fig. 4h). In addition, as shown in Fig. 4i, no obvious decrease in catalytic performance is found after 100 h, indicating the excellent stability of the Ni@NC catalyst in CO_2RR. These outperform most of the listed Ni-based catalysts (Table S2) in current density and stability. The excellent activity and stability of Ni@NC catalyst implies its high potentiality in producing CO from CO_2RR towards commercial application.

3.4. Identification of active sites for adsorption and activation of CO_2 molecules

Regarding the electrocatalyst in CO_2RR, the active sites for adsorption and activation of CO_2 molecules should be illustrated, which is crucial for the design and synthesis of excellent catalysts. By comparing the catalytic performance of M@C and M@NC catalysts, the C species can be excluded in the exploration of active sites. As for the Ni@NC catalyst, the surface metallic Ni particles, Ni–N_x single atom catalysts (SACs), and different N species (pyridinic-N, pyrrolic-N, and graphitic-N) are the potential active sites for CO_2 molecules [66–68]. Inspired by this thought, different control experiments are designed and performed for the identification of active sites.

First, the Ni@NC catalyst was subjected to acid-treatment for the removal the un-coated Ni particles (Fig. S13). As displayed in Fig. 5a,b, no obvious change in LSV curves and CO current density occurs after the removal of un-coated Ni particles, confirming that surface Ni particles are not the active sites for CO_2RR. To verify the possible role of Ni–N_x as active sites for CO_2RR, we used SCN$^-$ as an indicator to poison the metal-based sites [66,69]. No obvious change in current density is observed after the introduction of SCN$^-$ (Fig. 5a,b), thus excluding the possibility of Ni–N_x.

For further recognizing the active site of N species in Ni@NC, another control experiment was performed under the presence of H_3PO_4, which is well known to block pyridinic-N and pyrrolic-N sites in catalysts [54,70–72]. Concretely speaking, the $H_2PO_4^-$ ions dissociated from H_3PO_4 can protonate the pyridinic-N and pyrrolic-N. In addition, the PO_4^{3-} would block the positively charged carbon atoms adjacent to pyridinic-N and pyrrolic-N through electrostatic interaction and further stabilize the formed pyridinic N–H and pyrrolic N–H sites, thus causing pyridinic-N and pyrrolic-N sites inactive for adsorbing and activating CO_2 molecules. As shown in Fig. 5c and Fig. S14, the P species are successfully introduced, and the intensity of pyridinic-N and pyrrolic-N decreases after the introduction of H_3PO_4, indicating the blocking of pyridinic-N and pyrrolic-N sites. More importantly, the catalytic performance of Ni@NC after poisoning by H_3PO_4 shows obvious decrease compared with that of the fresh catalyst. For example, the CO current density decreases from 19.2 mA cm^{-2} to 11.5 mA cm^{-2} at -0.87 V, implying that the pyridinic-N or pyrrolic-N sites contribute to the CO_2RR.

For further excluding the role of metallic Ni particles and Ni–N_x, and identifying the role of pyridinic-N or pyrrolic-N, DFT calculations were taken to investigate the process of CO_2RR and HER over different active sites. Generally, CO_2RR has three elementary steps: the initial state (CO_2 molecule), adsorbed intermediate states (*COOH and *CO), and the final state (CO molecule). The free energy of *COOH and *CO reflects CO_2RR activity from the point of view of limiting potential. The desorption of *CO into gas phase also affects reactive performance. With regard to HER, which is the competitive reaction for CO_2RR, the free energy of *H and the desorption of *H into the gas phase influence HER and CO_2RR.

As shown in Fig. 5d,e, the formation of *COOH and *CO intermediate states is a downward process in the metallic Ni active site, and no energy
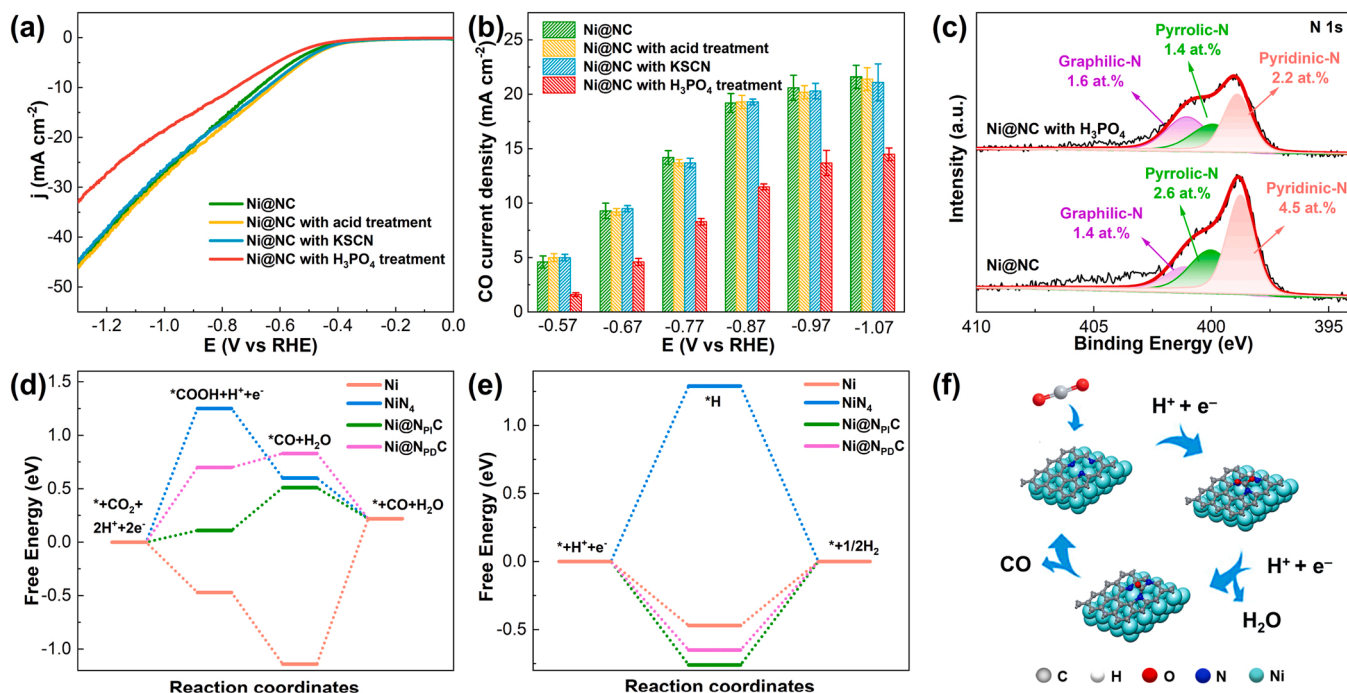
Fig. 5. (a) LSV test of Ni@NC, Ni@NC with acid treatment, Ni@NC with KSCN, and Ni@NC with H_3PO_4 treatment, (b) CO current density of Ni@NC, Ni@NC with acid treatment, Ni@NC with KSCN, and Ni@NC with H_3PO_4 treatment, (c) N 1 s XPS spectra before and after treatment with H_3PO_4. Free energy diagrams for (d) CO_2RR to CO and (e) HER process on Ni, NiN_4, Ni@N_{PI}C, and Ni@N_{PD}C active sites, (f) Illustration of the CO_2RR processes on Ni@NC catalysts.

needs to be overcome, resulting in the easy formation of *COOH and *CO intermediate states. By contrast, high energy (1.36 eV) exists in the transformation from *CO to CO, implying that the *CO desorption process is thermodynamically unfavorable and difficultly happens. As for the competitive reaction, the HER process only needs to overcome 0.50 eV, showing the easy occurrence of this process in the metallic Ni active site. In the NiN_4 active site, the formation of *COOH is the hardest step, and high free energy (1.25 eV) has to be overcome. As a result, the role of un-coated metal Ni particles and Ni–N_x SACs in CO_2RR can be excluded. These results further confirm the conclusion obtained from acid-treatment and SCN$^-$ poison experiment.

Moreover, the models of pyridinic-N (Ni@N_{PD}C) and pyrrolic-N (Ni@N_{PI}C) in Ni@NC active sites were established and investigated, and two active sites exhibit similar process. Specially, in the formation of *COOH intermediate state, 0.70 eV and 0.11 eV energy should be overcome in the Ni@N_{PD}C and Ni@N_{PI}C active sites. Subsequently, 0.83 eV and 0.51 eV need to be overcome for the formation of *CO intermediate state in Ni@N_{PD}C and Ni@N_{PI}C active sites. As a result, the CO_2RR is more likely to occur on Ni@N_{PI}C active sites than on Ni@N_{PD}C active sites, and Ni@N_{PI}C is the potential active site for CO_2RR (Fig. 5f).

3.5. Role of metal species

For further investigating the role of metal species in CO_2RR, the control experiments and DFT calculations were taken. The catalysts without metal nanoparticles (C and NC) were synthesized as the similar method and tested in CO_2RR. As shown in Fig. 6a,b and Fig. S15, the current density and FE of CO are enhanced with the introduction of N species, further confirming that N species can adsorb and activate CO_2 molecules. In addition, the catalytic performance of NC materials is lower than Co@NC and Ni@NC materials, implying the indispensability of metal nanoparticles in M@NC.

In the DFT calculations, the graphitic-C (C_G), Co@C_G, and Ni@C_G models were established and calculated in the CO_2RR and HER. As shown in Fig. 6c,d, the formation of *COOH needs a large energy (2.25 eV) for C_G. In addition, this step is the rate-determining step of

CO_2RR catalyzed by Co@C_G, and Ni@C_G, and 0.79 eV and 0.66 eV need to be conquered, respectively. With regards to the competitive reaction, HER only needs to overcome 0.39 eV and 0.25 eV for Co@C_G and Ni@C_G, meaning the easy occurrence of HER process. In conclusion, the Co@C_G and Ni@C_G catalysts mainly promote the HER process, and this conclusion is consistent with catalytic performance, which provides ~100% selectivity of H_2. In addition, the low energy for Ni@C_G implies the excellent catalytic performance in HER, consistent with the current density of HER (Fig. 4c,d).

As for the pyrrolic-N doped C (N_{PI}C), the formation of *COOH, *CO, and *H intermediate states easily occurs (Fig. 6e,f). However, high energy exists in the transformation from *CO to CO and *H to H_2, implying that the generation of CO and H_2 process is thermodynamically unfavorable and difficultly happen. In the Co@N_{PI}C and Ni@N_{PI}C catalysts, the desorption of *CO is thermodynamically favorable. In addition, the corresponding free energy for the generation of *CO and *COOH intermediate states is lower than that in M@C_G, implying that CO_2RR easily occurs on the Co@N_{PI}C and Ni@N_{PI}C catalysts. Furthermore, the HER process on Co@N_{PI}C and Ni@N_{PI}C catalysts was investigated. The formation of *H is thermodynamically favorable, and the desorption of *H is difficult, resulting in the difficulty in formation of H_2. Specifically speaking, the free energy for the formation of *CO is 0.40 eV and the desorption of *H to H_2 needs 0.76 eV in the Ni@N_{PI}C catalyst. Notably, the Ni@N_{PI}C catalyst is beneficial for CO_2RR, further confirming the catalytic results. With respect to the Co@N_{PI}C catalyst, the processes of *COOH to *CO (0.60 eV) and *H to H_2 (0.56 eV) need similar free energy, indicating that CO_2RR and HER can be simultaneously promoted by the Co@N_{PI}C catalyst. This conclusion is consistent with the catalytic activity, in which the CO and H_2 products are detected.

Meanwhile, with further decreased U (U = −0.5 V) below a critical limiting potential (Fig. S16), the elemental step of CO_2(g) to CO(g) in Ni@N_{PI}C becomes thermodynamically favorable. Hence, the CO_2RR can proceed on the pyrrolic-N active site in the Ni@N_{PI}C catalyst. As for HER, it can proceed on the C species in the Co@C_G and Ni@C_G catalysts.

Furthermore, the interaction mechanism between metal particles and N_{PI}C was also explored. The Fukui indices for radical attack values
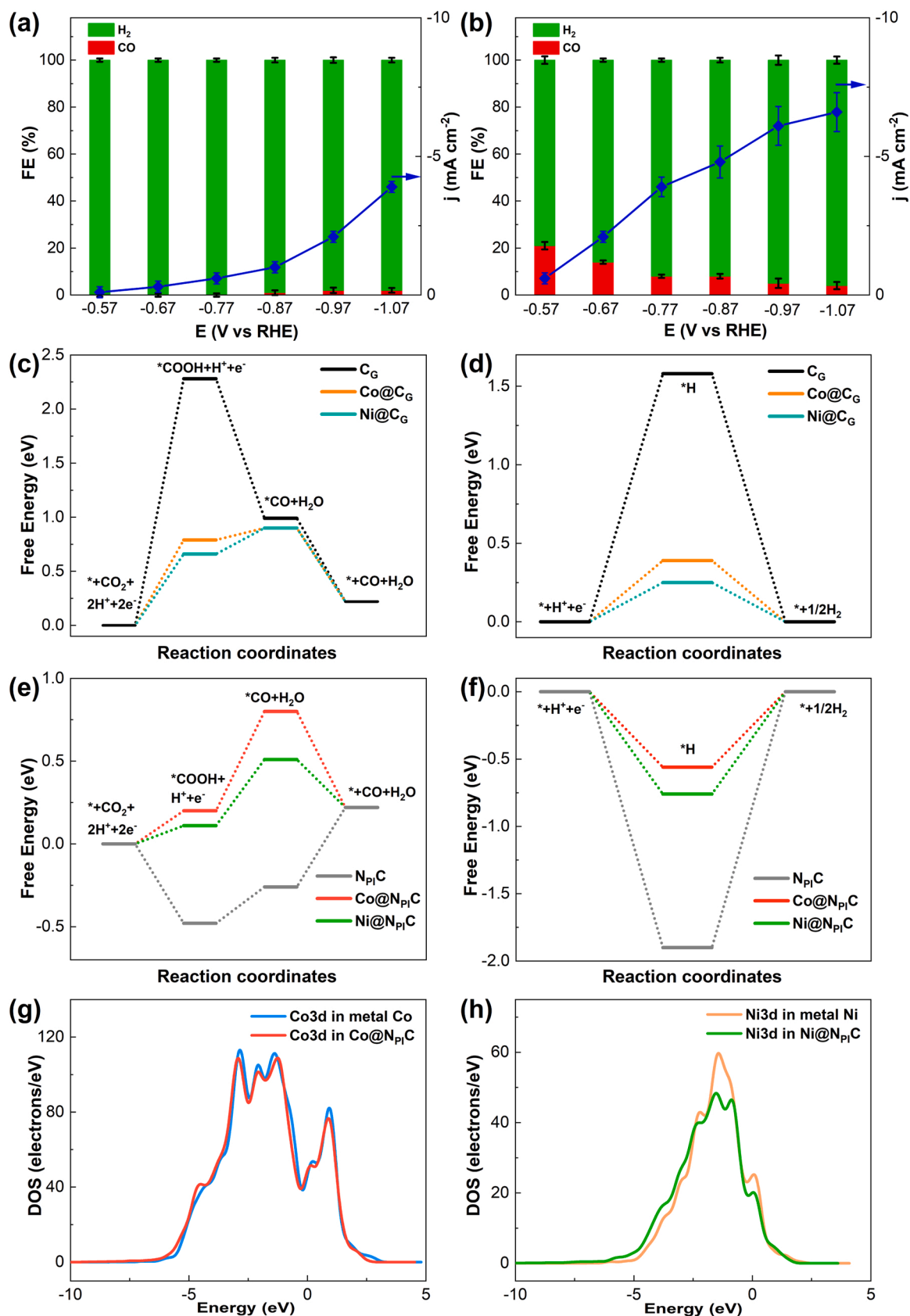
Fig. 6. Catalytic performance of (a) C and (b) NC catalysts. Free energy diagrams for (c) CO_2RR to CO and (d) HER process on C_G, $Co@C_G$, and $Ni@C_G$ active sites. Free energy diagrams for (e) CO_2RR to CO and (f) HER process on $N_{PI}C$, $Co@N_{PI}C$, and $Ni@N_{PI}C$ active sites. The PDOS for 3d orbitals of (g) metallic Co and $Co@N_{PI}C$, (h) metallic Ni and $Ni@N_{PI}C$.

were calculated and investigated [73]. Among the $N_{PI}C$, $Co@N_{PI}C$, and $Ni@N_{PI}C$ active sites, the $N_{PI}C$ has the largest value (0.059), implying that it has the strongest interaction with *COOH, *CO, and *H intermediate states, agreeing well with the results obtained from the DFT calculations (Fig. 6e,f), in which the $N_{PI}C$ active site is easy to interact with *COOH, *CO, and *H intermediate states. After the introduction of metal particles, the Fukui indices decrease to 0.017 and 0.012 for $Co@N_{PI}C$, and $Ni@N_{PI}C$, respectively, indicating decrease in the interactions between *COOH, *CO, and *H intermediate states and $N_{PI}C$ active site. Therefore, the catalytic performance of CO_2RR is successfully enhanced.

For further confirming the interaction between metal and pyrrolic-N active site, the partial density of states (PDOS) was used in investigating the electron structure of metal and $N_{PI}C$. As shown in Fig. 6g,h, the electron density of the 3d orbitals of metallic Co and Ni particles reduces as the formation of M@NC composite. In addition, the electron density of the π orbitals (−10 to −5 eV of 2p orbitals) of the N–C skeleton is enhanced (Fig. S17), indicating the transfer of electron from Co 3d and Ni 3d orbitals to π orbitals of the N–C skeleton. As a consequence, the electron density of the N–C skeleton is increased, and interaction between pyrrolic-N active site and *COOH, *CO, and *H intermediate states is improved. Moreover, in the comparison between $Co@N_{PI}C$ and $Ni@N_{PI}C$, more electrons are transferred from Ni to $N_{PI}C$. As a result, the $Ni@N_{PI}C$ exhibits higher CO_2RR activity than $Co@N_{PI}C$.

4. Conclusion

In this work, different kinds of metal nanoparticles encapsulated within carbon shells (Co@C, Co@NC, Ni@C, and Ni@NC) were achieved and employed in CO_2RR. The Ni@NC material exhibited high CO_2 reduction activity and stability, indicating its high potentiality in producing CO from CO_2RR toward commercial application. As confirmed by the control experiments and DFT calculations, the pyrrolic-N active site in Ni@NC was confirmed. The metal nanoparticles improve the electronic structure of N species, thereby decreasing their ability for radical attack (*COOH and *CO) and improving their catalytic performance in CO_2RR. Consequently, this work clarifies the role of metal and N species in M@NC catalysts and provides a reference for designing M@NC catalyst for CO_2RR to CO.

CRediT authorship contribution statement

Manfen Liang: Investigation, Methodology, Formal analysis, Writing – original draft. **Yu Liu:** Methodology, Data curation. **Jie Zhang:** Methodology, Data curation. **Fangyuan Wang:** Data curation. **Zhichao Miao:** Methodology, Formal analysis, Writing – review & editing, Funding acquisition. **Lechen Diao:** Writing – review & editing. **Jinglin Mu:** Methodology, Visualization, Data curation, Software. **Jin Zhou:** Funding acquisition, Resources. **Shuping Zhuo:** Funding acquisition, Resources.

Declaration of Competing Interest

The authors declare that they have no known competing financial interests or personal relationships that could have appeared to influence the work reported in this paper.

Acknowledgements

Appendix A. Supporting information

Supplementary data associated with this article can be found in the online version at doi:10.1016/j.apcatb.2022.121115.

References

[1] Y.Y. Birdja, E. Pérez-Gallent, M.C. Figueiredo, A.J. Göttle, F. Calle-Vallejo, M.T. M. Koper, Advances and challenges in understanding the electrocatalytic conversion of carbon dioxide to fuels, Nat. Energy 4 (2019) 732–745, https://doi.org/10.1038/s41560-019-0450-y.

[2] L. Fan, C. Xia, F. Yang, J. Wang, H. Wang, Y. Lu, Strategies in catalysts and electrolyzer design for electrochemical CO_2 reduction toward C_{2+} products, Sci. Adv. 6 (2020) eaay3111, https://doi.org/10.1126/sciadv.aay3111.

[3] D. Ješić, D. Lašič Jurković, A. Pohar, L. Suhadolnik, B. Likozar, Engineering photocatalytic and photoelectrocatalytic CO_2 reduction reactions: mechanisms, intrinsic kinetics, mass transfer resistances, reactors and multi-scale modelling simulations, Chem. Eng. J. 407 (2021), 126799, https://doi.org/10.1016/j.cej.2020.126799.

[4] H. Zhou, Z. Chen, E. Kountoupi, A. Tsoukalou, P.M. Abdala, P. Florian, A. Fedorov, C.R. Muller, Two-dimensional molybdenum carbide 2D-Mo_2C as a superior catalyst for CO_2 hydrogenation, Nat. Commun. 12 (2021) 5510, https://doi.org/10.1038/s41467-021-25784-0.

[5] A. Alissandratos, H.K. Kim, C.J. Easton, Formate production through carbon dioxide hydrogenation with recombinant whole cell biocatalysts, Bioresour. Technol. 164 (2014) 7–11, https://doi.org/10.1016/j.biortech.2014.04.064.

[6] S. Liu, X.F. Lu, J. Xiao, X. Wang, X.W. Lou, Bi_2O_3 nanosheets grown on multi-channel carbon matrix catalyze efficient CO_2 electroreduction to HCOOH, Angew. Chem. Int. Ed. 58 (2019) 13828–13833, https://doi.org/10.1002/anie.201907674.

[7] L.R.L. Ting, O. Piqué, S.Y. Lim, M. Tanhaei, F. Calle-Vallejo, B.S. Yeo, Enhancing CO_2 electroreduction to ethanol on copper–silver composites by opening an alternative catalytic pathway, ACS Catal. 10 (2020) 4059–4069, https://doi.org/10.1021/acscatal.9b05319.

[8] S. Lamaison, D. Wakerley, D. Montero, G. Rousse, D. Taverna, D. Giaume, D. Mercier, J. Blanchard, H.N. Tran, M. Fontecave, V. Mougel, Zn–Cu alloy nanofoams as efficient catalysts for the reduction of CO_2 to syngas mixtures with a potential-independent H_2/CO ratio, ChemSusChem 12 (2019) 511–517, https://doi.org/10.1002/cssc.201802287.

[9] D.U. Nielsen, X.M. Hu, K. Daasbjerg, T. Skrydstrup, Chemically and electrochemically catalysed conversion of CO_2 to CO with follow-up utilization to value-added chemicals, Nat. Catal. 1 (2018) 244–254, https://doi.org/10.1038/s41929-018-0051-3.

[10] N. Morlanés, K. Takanabe, V. Rodionov, Simultaneous reduction of CO_2 and splitting of H_2O by a single immobilized cobalt phthalocyanine electrocatalyst, ACS Catal. 6 (2016) 3092–3095, https://doi.org/10.1021/acscatal.6b00543.

[11] C. Hu, S. Bai, L. Gao, S. Liang, J. Yang, S.D. Cheng, S.B. Mi, J. Qiu, Porosity-induced high selectivity for CO_2 electroreduction to CO on Fe-doped ZIF-derived carbon catalysts, ACS Catal. 9 (2019) 11579–11588, https://doi.org/10.1021/acscatal.9b03175.

[12] W. Zhu, Y.J. Zhang, H. Zhang, H. Lv, Q. Li, R. Michalsky, A.A. Peterson, S. Sun, Active and selective conversion of CO_2 to CO on ultrathin Au nanowires, J. Am. Chem. Soc. 136 (2014) 16132–16135, https://doi.org/10.1021/ja5095099.

[13] Y.C. Li, G. Lee, T. Yuan, Y. Wang, D.H. Nam, Z. Wang, F.P. García de Arquer, Y. Lum, C.T. Dinh, O. Voznyy, E.H. Sargent, CO2 electroreduction from carbonate electrolyte, ACS Energy Lett. 4 (2019) 1427–1431, https://doi.org/10.1021/acsenergylett.9b00975.

[14] G.W. Woyessa, J.B. Cruz, M. Rameez, C.H. Hung, Nanocomposite catalyst of graphitic carbon nitride and Cu/Fe mixed metal oxide for electrochemical CO_2 reduction to CO, Appl. Catal. B Environ. 291 (2021) 120052, https://doi.org/10.1016/j.apcatb.2021.120052.

[15] R. He, A. Zhang, Y. Ding, T. Kong, Q. Xiao, H. Li, Y. Liu, J. Zeng, Achieving the widest range of syngas proportions at high current density over cadmium sulfoselenide nanorods in CO_2 electroreduction, Adv. Mater. 30 (2018) 1705872, https://doi.org/10.1002/adma.201705872.

[16] A.S. Varela, W. Ju, A. Bagger, P. Franco, J. Rossmeisl, P. Strasser, Electrochemical reduction of CO_2 on metal-nitrogen-doped carbon catalysts, ACS Catal. 9 (2019) 7270–7284, https://doi.org/10.1021/acscatal.9b01405.

[17] W. Ju, A. Bagger, G.P. Hao, A.S. Varela, I. Sinev, V. Bon, B. Roldan Cuenya, S. Kaskel, J. Rossmeisl, P. Strasser, Understanding activity and selectivity of metal-nitrogen-doped carbon catalysts for electrochemical reduction of CO_2, Nat. Commun. 8 (2017) 944, https://doi.org/10.1038/s41467-017-01035-z.

[18] L. Dai, Q. Qin, P. Wang, X. Zhao, C. Hu, P. Liu, R. Qin, M. Chen, D. Ou, C. Xu, S. Mo, B. Wu, G. Fu, P. Zhang, N. Zheng, Ultrastable atomic copper nanosheets for selective electrochemical reduction of carbon dioxide, Sci. Adv. 3 (2017), e1701069, https://doi.org/10.1126/sciadv.1701069.

[19] P.P. Sharma, J. Wu, R.M. Yadav, M. Liu, C.J. Wright, C.S. Tiwary, B.I. Yakobson, J. Lou, P.M. Ajayan, X.D. Zhou, Nitrogen-doped carbon nanotube arrays for high-efficiency electrochemical reduction of CO_2: on the understanding of defects, defect density, and selectivity, Angew. Chem. Int. Ed. 127 (2015) 13905–13909, https://doi.org/10.1002/anie.201506062.

[20] L. Ye, Y. Ying, D. Sun, Z. Zhang, L. Fei, Z. Wen, J. Qiao, H. Huang, Highly efficient porous carbon electrocatalyst with controllable N-species content for selective CO_2 reduction, Angew. Chem. Int. Ed. 59 (2020) 3244–3251, https://doi.org/10.1002/anie.201912751.

[21] S. Back, M.S. Yeom, Y. Jung, Active sites of Au and Ag nanoparticle catalysts for CO_2 electroreduction to CO, ACS Catal. 5 (2015) 5089–5096, https://doi.org/10.1021/acscatal.5b00462.

[22] M. Ma, B.J. Trzesniewski, J. Xie, W.A. Smith, Selective and efficient reduction of carbon dioxide to carbon monoxide on oxide-derived nanostructured silver electrocatalysts, Angew. Chem. Int. Ed. 128 (2016) 9900–9904, https://doi.org/10.1002/anie.201604654.

[23] H.Y. Jeong, M. Balamurugan, V.S.K. Choutipalli, E. Jeong, V. Subramanian, U. Sim, K.T. Nam, Achieving highly efficient CO_2 to CO electroreduction exceeding 300 mA cm^{-2} with single-atom nickel electrocatalysts, J. Mater. Chem. A 7 (2019) 10651–10661, https://doi.org/10.1039/c9ta02405k.

[24] C. He, Y. Zhang, Y. Zhang, L. Zhao, L.P. Yuan, J. Zhang, J. Ma, J.S. Hu, Molecular evidence for metallic cobalt boosting CO_2 electroreduction on pyridinic nitrogen, Angew. Chem. Int. Ed. 132 (2020) 4944–4949, https://doi.org/10.1002/anie.201916520 10.1002/ange.201916520.

[25] Y. Li, S.L. Zhang, W. Cheng, Y. Chen, D. Luan, S. Gao, X.W. Lou, Loading single-Ni atoms on assembled hollow N-rich carbon plates for efficient CO_2 electroreduction, Adv. Mater. 34 (2022), 2105204, https://doi.org/10.1002/adma.202105204.

[26] S. Li, M. Ceccato, X. Lu, S. Frank, N. Lock, A. Roldan, X.M. Hu, T. Skrydstrup, K. Daasbjerg, Incorporation of nickel single atoms into carbon paper as self-standing electrocatalyst for CO_2 reduction, J. Mater. Chem. A 9 (2021) 1583–1592, https://doi.org/10.1039/d0ta08433f.

[27] C.Z. Yuan, H.B. Li, Y.F. Jiang, K. Liang, S.J. Zhao, X.X. Fang, L.B. Ma, T. Zhao, C. Lin, A.W. Xu, Tuning the activity of N-doped carbon for CO_2 reduction via in situ encapsulation of nickel nanoparticles into nano-hybrid carbon substrates, J. Mater. Chem. A 7 (2019) 6894–6900, https://doi.org/10.1039/c8ta11500a.

[28] Y. He, Y. Li, J. Zhang, S. Wang, D. Huang, G. Yang, X. Yi, H. Lin, X. Han, W. Hu, Y. Deng, J. Ye, Low-temperature strategy toward Ni-NC@Ni core-shell nanostructure with single-Ni sites for efficient CO_2 electroreduction, Nano Energy 77 (2020), 105010, https://doi.org/10.1016/j.nanoen.2020.105010.

[29] D. Zhu, Y. Huang, R. Li, T. Huang, J. Cao, Z. Shen, S.C. Lee, Formaldehyde oxidation over Co@N-doped carbon at room temperature: tunable Co size and intensified surface electron density, ACS ES&T Eng. 1 (2021) 917–927, https://doi.org/10.1021/acsestengg.1c00080.

[30] S. Liang, Q. Jiang, Q. Wang, Y. Liu, Revealing the real role of decorated nitrogen-doped carbon catalysts for electrochemical reduction of CO_2 to CO, Adv. Energy Mater. 11 (2021), 2101477, https://doi.org/10.1002/aenm.202101477.

[31] D.M. Koshy, S. Chen, D.U. Lee, M.B. Stevens, A.M. Abdellah, S.M. Dull, G. Chen, D. Nordlund, A. Gallo, C. Hahn, D.C. Higgins, Z. Bao, T.F. Jaramillo, Understanding the origin of highly selective CO_2 electroreduction to CO on Ni,N-doped carbon catalysts, Angew. Chem. Int. Ed. 132 (2020) 4072–4079, https://doi.org/10.1002/anie.201912857.

[32] K. Iwase, K. Ebner, J.S. Diercks, V.A. Saveleva, S. Unsal, F. Krumeich, T. Harada, I. Honma, S. Nakanishi, K. Kamiya, T.J. Schmidt, J. Herranz, Effect of cobalt speciation and the graphitization of the carbon matrix on the CO_2 electroreduction activity of Co/N-doped carbon materials, ACS Appl. Mater. Interfaces 13 (2021) 15122–15131, https://doi.org/10.1021/acsami.0c21920.

[33] J. Meng, C. Niu, L. Xu, J. Li, X. Liu, X. Wang, Y. Wu, X. Xu, W. Chen, Q. Li, Z. Zhu, D. Zhao, L. Mai, General oriented formation of carbon nanotubes from metal-organic frameworks, J. Am. Chem. Soc. 139 (2017) 8212–8221, https://doi.org/10.1021/jacs.7b01942.

[34] J. Qin, S. Wang, X. Wang, Visible-light reduction CO_2 with dodecahedral zeolitic imidazolate framework ZIF-67 as an efficient co-catalyst, Appl. Catal. B Environ. 209 (2017) 476–482, https://doi.org/10.1016/j.apcatb.2017.03.018.

[35] S.L. Zacho, J. Mielby, S. Kegnæs, Hydrolytic dehydrogenation of ammonia borane over ZIF-67 derived Co nanoparticle catalysts, Catal. Sci. Technol. 8 (2018) 4741–4746, https://doi.org/10.1039/C8CY01500G 10.1039/x0xx00000x.

[36] X. Jiang, H. Li, S. Li, S. Huang, C. Zhu, L. Hou, Metal-organic framework-derived Ni–Co alloy@carbon microspheres as high-performance counter electrode catalysts for dye-sensitized solar cells, Chem. Eng. J. 334 (2018) 419–431, https://doi.org/10.1016/j.cej.2017.10.043.

[37] Y. Qiu, Y. Lin, H. Yang, L. Wang, M. Wang, B. Wen, Hollow Ni/C microspheres derived from Ni-metal organic framework for electromagnetic wave absorption, Chem. Eng. J. 383 (2020), 123207, https://doi.org/10.1016/j.cej.2019.123207.

[38] B. Delley, An all-electron numerical method for solving the local density functional for polyatomic molecules, J. Chem. Phys. 92 (1990) 508–517, https://doi.org/10.1063/1.458452.

[39] B. Delley, From molecules to solids with the DMol$_3$ approach, J. Chem. Phys. 113 (2000) 7756–7764, https://doi.org/10.1063/1.1316015.

[40] M. Jia, C. Choi, T.S. Wu, C. Ma, P. Kang, H. Tao, Q. Fan, S. Hong, S. Liu, Y.L. Soo, Y. Jung, J. Qiu, Z. Sun, Carbon-supported Ni nanoparticles for efficient CO_2 electroreduction, Chem. Sci. 9 (2018) 8775–8780, https://doi.org/10.1039/c8sc03732a.

[41] Z. Li, D. He, X. Yan, S. Dai, S. Younan, Z. Ke, X. Pan, X. Xiao, H. Wu, J. Gu, Size-dependent nickel-based electrocatalysts for selective CO_2 reduction, Angew. Chem. Int. Ed. 59 (2020) 18572–18577, https://doi.org/10.1002/anie.202000318.

[42] J. Long, R. Li, X. Gou, Well-organized Co-Ni@NC material derived from hetero-dinuclear MOFs as efficient electrocatalysts for oxygen reduction, Catal. Commun. 95 (2017) 31–35, https://doi.org/10.1016/j.catcom.2017.02.026.

[43] J. Zhao, X. Quan, S. Chen, Y. Liu, H. Yu, Cobalt nanoparticles encapsulated in porous carbons derived from core-shell ZIF67@ZIF8 as efficient electrocatalysts for oxygen evolution reaction, ACS Appl. Mater. Interfaces 9 (2017) 28685–28694, https://doi.org/10.1021/acsami.7b10138.

[44] Y. Hou, T. Huang, Z. Wen, S. Mao, S. Cui, J. Chen, Metal−organic framework-derived nitrogen-doped core-shell-structured porous Fe/Fe$_3$C@C nanoboxes

[45] supported on graphene sheets for efficient oxygen reduction reactions, Adv. Energy Mater. 4 (2014), 1400337, https://doi.org/10.1002/aenm.201400337.

[45] C. Yan, Y. Ye, L. Lin, H. Wu, Q. Jiang, G. Wang, X. Bao, Improving CO_2 electroreduction over ZIF-derived carbon doped with Fe–N sites by an additional ammonia treatment, Catal. Today 330 (2019) 252–258, https://doi.org/10.1016/j.cattod.2018.03.062.

[46] R. Senthil Kumar, S. Senthil Kumar, M. Anbu Kulandainathan, Efficient electrosynthesis of highly active Cu$_3$(BTC)$_2$-MOF and its catalytic application to chemical reduction, Microporous Mesoporous Mater. 168 (2013) 57–64, https://doi.org/10.1016/j.micromeso.2012.09.028.

[47] D. Ding, K. Shen, X. Chen, H. Chen, J. Chen, T. Fan, R. Wu, Y. Li, Multi-level architecture optimization of MOF-templated Co-based nanoparticles embedded in hollow N-doped carbon polyhedra for efficient OER and ORR, ACS Catal. 8 (2018) 7879–7888, https://doi.org/10.1021/acscatal.8b02504.

[48] H. Li, J. Wan, Y. Ma, Y. Wang, X. Chen, Z. Guan, Degradation of refractory dibutyl phthalate by peroxymonosulfate activated with novel catalysts cobalt metal-organic frameworks: mechanism, performance, and stability, J. Hazard. Mater. 318 (2016) 154–163, https://doi.org/10.1016/j.jhazmat.2016.06.058.

[49] Q. Gan, H. He, K. Zhao, Z. He, S. Liu, Morphology-dependent electrochemical performance of Ni-1,3,5-benzenetricarboxylate metal-organic frameworks as an anode material for Li-ion batteries, J. Colloid Interface Sci. 530 (2018) 127–136, https://doi.org/10.1016/j.jcis.2018.06.057.

[50] Z. Mohammadpour, H.R. Zare, Fabrication of a pH-sensitive epoxy nanocomposite coating based on a Zn-BTC metal-organic framework containing benzotriazole as a smart corrosion inhibitor, Cryst. Growth Des. 21 (2021) 3954–3966, https://doi.org/10.1021/acs.cgd.1c00284.

[51] Y. Zhu, Z. Zhang, J. Cheng, H. Guo, W. Yang, Ni-BTC metal-organic framework loaded on MCM-41 to promote hydrodeoxygenation and hydrocracking in jet biofuel production, Int. J. Hydrog. Energy 46 (2021) 3898–3908, https://doi.org/10.1016/j.ijhydene.2020.10.216.

[52] G. Zhou, D.W. Wang, L.C. Yin, N. Li, F. Li, H.M. Cheng, Oxygen bridges between NiO nanosheets and graphene for improvement of lithium storage, ACS Nano 6 (2012) 3214–3223, https://doi.org/10.1021/nn300098m.

[53] X.H. Xia, J.P. Tu, J. Zhang, X.L. Wang, W.K. Zhang, H. Huang, Electrochromic properties of porous NiO thin films prepared by a chemical bath deposition, Sol. Energy Mater. Sol. Cells 92 (2008) 628–633, https://doi.org/10.1016/j.solmat.2008.01.009.

[54] Y. Niu, C. Zhang, Y. Wang, D. Fang, L. Zhang, C. Wang, Confining chainmail-bearing Ni nanoparticles in N-doped carbon nanotubes for robust and efficient electroreduction of CO_2, ChemSusChem 14 (2021) 1140–1154, https://doi.org/10.1002/cssc.202002596.

[55] T.A. Al-Attas, N.N. Marei, X. Yong, N.G. Yasri, V. Thangadurai, G. Shimizu, S. Siahrostami, M.G. Kibria, Ligand-engineered metal–organic frameworks for electrochemical reduction of carbon dioxide to carbon monoxide, ACS Catal. 11 (2021) 7350–7357, https://doi.org/10.1021/acscatal.1c01506.

[56] Y. Liu, H. Jiang, Y. Zhu, X. Yang, C. Li, Transition metals (Fe, Co, and Ni) encapsulated in nitrogen-doped carbon nanotubes as bi-functional catalysts for oxygen electrode reactions, J. Mater. Chem. A 4 (2016) 1694–1701, https://doi.org/10.1039/c5ta10551j.

[57] Z. Ma, C. Tsounis, P.V. Kumar, Z. Han, R.J. Wong, C.Y. Toe, S. Zhou, N.M. Bedford, L. Thomsen, Y.H. Ng, R. Amal, Enhanced electrochemical CO_2 reduction of Cu@Cu$_x$O nanoparticles decorated on 3D vertical graphene with intrinsic sp^3-type defect, Adv. Funct. Mater. 30 (2020), 1910118, https://doi.org/10.1002/adfm.201910118.

[58] B. Zhang, Z. Guo, Z. Zuo, W. Pan, J. Zhang, The ensemble effect of nitrogen doping and ultrasmall SnO$_2$ nanocrystals on graphene sheets for efficient electroreduction of carbon dioxide, Appl. Catal. B Environ. 239 (2018) 441–449, https://doi.org/10.1016/j.apcatb.2018.08.044.

[59] M. Thommes, K. Kaneko, A.V. Neimark, J.P. Olivier, F. Rodriguez-Reinoso, J. Rouquerol, K.S.W. Sing, Physisorption of gases, with special reference to the evaluation of surface area and pore size distribution (IUPAC Technical Report), Pure Appl. Chem. 87 (2015) 1051–1069, https://doi.org/10.1515/pac-2014-1117.

[60] W. Xiong, J. Yang, L. Shuai, Y. Hou, M. Qiu, X. Li, M.K.H. Leung, CuSn alloy nanoparticles on nitrogen-doped graphene for electrocatalytic CO_2 reduction, ChemElectroChem 6 (2019) 5951–5957, https://doi.org/10.1002/celc.201901381.

[61] C. Cui, Y. Liu, S. Mehdi, H. Wen, B. Zhou, J. Li, B. Li, Enhancing effect of Fe-doping on the activity of nano Ni catalyst towards hydrogen evolution from NH$_3$BH$_3$, Appl. Catal. B Environ. 265 (2020), 118612, https://doi.org/10.1016/j.apcatb.2020.118612.

[62] C. Chen, X. Sun, X. Yan, Y. Wu, H. Liu, Q. Zhu, B.B.A. Bediako, B. Han, Boosting CO_2 electroreduction on N,P-Co-doped carbon aerogels, Angew. Chem. Int. Ed. 59 (2020) 11123–11129, https://doi.org/10.1002/anie.200004226.

[63] C. Hu, Y. Mu, S. Bai, J. Yang, L. Gao, S.D. Cheng, S.B. Mi, J. Qiu, Polyvinyl pyrrolidone mediated fabrication of Fe, N-codoped porous carbon sheets for efficient electrocatalytic CO_2 reduction, Carbon 153 (2019) 609–616, https://doi.org/10.1016/j.carbon.2019.07.071.

[64] C. Wang, X. Hu, X. Hu, X. Liu, Q. Guan, R. Hao, Y. Liu, W. Li, Typical transition metal single-atom catalysts with a metal-pyridine N structure for efficient CO_2 electroreduction, Appl. Catal. B Environ. 296 (2021) 120331, https://doi.org/10.1016/j.apcatb.2021.120331.

[65] W.H. Cheng, M.H. Richter, I. Sullivan, D.M. Larson, C. Xiang, B.S. Brunschwig, H.A. Atwater, CO_2 reduction to CO with 19% efficiency in a solar-driven gas diffusion electrode flow cell under outdoor solar illumination, ACS Energy Lett. 5 (2020) 470–476, https://doi.org/10.1021/acsenergylett.9b02576.

[66] X. Wang, X. Sang, C.L. Dong, S. Yao, L. Shuai, J. Lu, B. Yang, Z. Li, L. Lei, M. Qiu, L. Dai, Y. Hou, Proton capture strategy for enhancing electrochemical CO_2 reduction on atomically dispersed metal-nitrogen active sites, Angew. Chem. Int. Ed. 60 (2021) 11959–11965, https://doi.org/10.1002/anie.202100011.

[67] Q. Fan, P. Hou, C. Choi, T.S. Wu, S. Hong, F. Li, Y.L. Soo, P. Kang, Y. Jung, Z. Sun, Activation of Ni particles into single Ni–N atoms for efficient electrochemical reduction of CO_2, Adv. Energy Mater. 10 (2019), 1903068, https://doi.org/10.1002/aenm.201903068.

[68] Z. Miao, J. Meng, M. Liang, Z. Li, Y. Zhao, F. Wang, L. Xu, J. Mu, S. Zhuo, J. Zhou, In-situ CVD synthesis of Ni@N–CNTs/carbon paper electrode for electro-reduction of CO_2, Carbon 172 (2021) 324–333, https://doi.org/10.1016/j.carbon.2020.10.044.

[69] F. Pan, W. Deng, C. Justiniano, Y. Li, Identification of champion transition metals centers in metal and nitrogen-codoped carbon catalysts for CO_2 reduction, Appl. Catal. B Environ. 226 (2018) 463–472, https://doi.org/10.1016/j.apcatb.2018.01.001.

[70] J. Li, W.Y. Zan, H. Kang, Z. Dong, X. Zhang, Y. Lin, Y.W. Mu, F. Zhang, X.M. Zhang, J. Gu, Graphitic-N highly doped graphene-like carbon: a superior metal-free catalyst for efficient reduction of CO_2, Appl. Catal. B Environ. 298 (2021) 120510, https://doi.org/10.1016/j.apcatb.2021.120510.

[71] S. Liu, H. Yang, X. Huang, L. Liu, W. Cai, J. Gao, X. Li, T. Zhang, Y. Huang, B. Liu, Identifying active sites of nitrogen-doped carbon materials for the CO_2 reduction reaction, Adv. Funct. Mater. 28 (2018) 1800499, https://doi.org/10.1002/adfm.201800499.

[72] K. Mamtani, D. Jain, D. Zemlyanov, G. Celik, J. Luthman, G. Renkes, A.C. Co, U. S. Ozkan, Probing the oxygen reduction reaction active sites over nitrogen-doped carbon nanostructures (CN_x) in acidic media using phosphate anion, ACS Catal. 6 (2016) 7249–7259, https://doi.org/10.1021/acscatal.6b01786.

[73] W. Yang, W.J. Mortier, The use of global and local molecular parameters for the analysis of the gas-phase basicity of amines, J. Am. Chem. Soc. 108 (1986) 5708–5711, https://doi.org/10.1021/ja00279a008.